Avoided Curve Crossing between the A$_1$ and B$_1$ States in CF$_2$Br$_2$ Photolysis at 234 and 265 nm[†]

Moon Soo Park, Tae Kyu Kim, Sung-Hae Lee, and Kyung-Hoon Jung*

Department of Chemistry and School of Molecular Science (BK21), Korea Advanced Institute of Science and Technology, Taeduck Science Town, Taejon 305-701, Korea
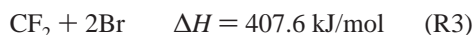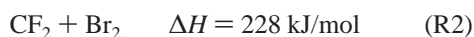
Hans-Robert Volpp and Jürgen Wolfrum

Physikalisch-Chemisches Institut der Universität Heidelberg, Im Neuenheimer Feld 253, D-69120, Heidelberg, Germany

The photodissociation dynamics of CF$_2$Br$_2$ has been studied using a two-dimensional photofragment ion image technique for the two excitation wavelengths 234 and 265 nm. At 234 nm, three dissociation channels, i.e., the radical CF$_2$Br + Br (^{2}P$_J$) (J = $^1/_2$, $^3/_2$), the three-body CF$_2$ + 2Br (^{2}P$_J$) (J = $^1/_2$, $^3/_2$), and the molecular elimination channel CF$_2$ + Br$_2$, were observed with quantum yields of 0.84, 0.15, and trace, respectively. The difference between β (CF$_2$Br + Br (^{2}P$_{3/2}$)) = 0.65 and β (CF$_2$Br + Br (^{2}P$_{1/2}$)) = 0.80 suggests that the excited A$_1$ and B$_1$ states are strongly correlated by avoided curve crossing with a probability of 0.78. At 265 nm, the radical channel, the observed major primary dissociation channel, shows several components due to the transition close to the curve crossing point. On the basis of observations at both wavelengths, we have proposed a photodissociation dynamics model of CF$_2$Br$_2$ after A-band excitation.

1. Introduction

CF$_2$Br$_2$, a frequently used fire retardant, is a strong ozone depleting reagent in the stratosphere.[1] The A-band photodissociation of CF$_2$Br$_2$, centered at 230 nm in Figure 1,[2] exhibits a complex multichannel photochemistry. Three primary channels, i.e., radical (R1), molecular elimination (R2), and three-body dissociation channels (R3), are attainable energetically in the A-band.[3−11]

$$CF_2Br_2 + h\nu \rightarrow CF_2Br + Br \qquad \Delta H = 247.6 \text{ kJ/mol} \quad (R1)$$

$$CF_2 + Br_2 \qquad \Delta H = 228 \text{ kJ/mol} \qquad (R2)$$

$$CF_2 + 2Br \qquad \Delta H = 407.6 \text{ kJ/mol} \qquad (R3)$$

The CF$_2$Br radical formed through the radical channel can undergo further photodissociation (R4) or unimolecular decay of internally hot radicals (R5).

$$CF_2Br + h\nu \rightarrow CF_2 + Br \qquad (R4)$$

$$CF_2Br^\ddagger \rightarrow CF_2 + Br \qquad (R5)$$
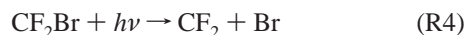
These channels are further resolved realizing the ground Br (4p ^{2}P$_{3/2}$) and the spin−orbit (SO) excited-state Br* (4p ^{2}P$_{1/2}$), where the SO coupling energy, E_{so} (Br − Br*) = 44.1 kJ/mol. The [2 + 1] resonance enhanced multiphoton ionization (REMPI) time-of-flight (TOF) image technique is adopted in the present study, since it allows Br and Br* fragments to be selectively monitored and can also be used to study the vector
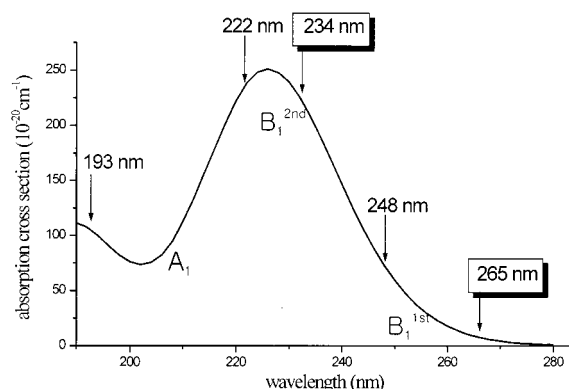
Figure 1. Absorption cross-section of CF$_2$Br$_2$ in the UV region. This spectrum has been established by using the data available in ref 2.

quantities of the photofragments. Photodissociation studies of CF$_2$Br$_2$ have been performed at 193 and 248 nm using the rotatable mass spectrometric technique.[4,5] The radical channel was the only observed primary photodissociation channel in the 248-nm photolysis experiments, while both the radical and the molecular elimination channels were observed at 193 nm. The bromine atom product quantum yield obtained by fluorescence detection at 222 nm has been found to be 1.63, suggesting the presence of three-body dissociation channel after excitation in the center of the A-band.[6] The electronically excited CF$_2$ (Ã) radical has been produced through the secondary photodissociation at 248 nm.[7−9]

Earlier studies of its iodine homologues, CH$_2$I$_2$ and CF$_2$I$_2$, may be instructive to understand the photodissociation of CF$_2$Br$_2$. In the CH$_2$I$_2$ photolysis, the radical channel was found to be dominant over the whole wavelength range of the A-band,[12−18] and very small amounts of I$_2$ formed through the molecular elimination channel were observed. The three-body

Photodissociation Dynamics of CF$_2$Br$_2$

J. Phys. Chem. A, Vol. 105, No. 23, 2001 **5607**

dissociation channel was not observed because of its large dissociation energy. The photodissociation of CF$_2$I$_2$ has shown a smooth transition from an exclusive radical channel at the red edge of the A-band to an exclusive concerted three-body channel at the blue edge, with no molecular elimination channel observed.[16-18] The I*($^2P_{1/2}$)/I($^2P_{3/2}$) branching ratio has shown the increasing propensity with the photolysis energy increase in iodine atom formation via the radical channel from both CH$_2$I$_2$ and CF$_2$I$_2$. The photolysis energy dependence of I*/I has suggested that at least two excited states are related in the radical channel interacting with each other by an electronic curve-crossing. The interaction between the excited state potential energy surfaces (PES), however, has not yet been fully understood in the photolysis of CX$_2$Y$_2$ (X = H, F, Y = Br, I) type molecules. Additional information is needed to draw a quantitative picture of the competition between the three primary channels and the interaction between these excited-state PES's after A-band excitation.

In the present study we have investigated the photodissociation dynamics of CF$_2$Br$_2$ at the 234 and 265 nm photolysis wavelengths adopting the [2 + 1] REMPI TOF technique to investigate the interaction of the excited states and the competition between the three primary product channels (R1−R3).

2. Experimental Section

The reaction chamber coupled with a supersonic molecular beam source and a TOF mass spectrometer was used in the present study and described in detail elsewhere.[19] In brief, the beam source chamber is constructed based on an 8-in. stainless steel tee and nipple-type chambers. Sample mixture was introduced into the source chamber through a molecular beam valve (General Valve) with an 800 μm diameter orifice. The valve was operated typically at 10 Hz with a pulse width of 200 μs. The source chamber was pumped with an 8-in. oil diffusion pump (Alcatel, 6250) to ca. 1 x 10^{-5} Torr during the operation of the molecular beam. A conical skimmer with an 800-μm diameter orifice skimmed the molecular beam at 20 mm downstream of the valve. The skimmer separates the TOF mass spectrometer from the molecular beam source chamber. The beam passed through the skimmer and was then collimated by a 1-mm diameter pinhole before entering the ionization region of the main chamber. The TOF mass spectrometer is installed in the main chamber composed of an 8-in. cube and a flight tube. The main chamber was pumped to a pressure of 5 x 10^{-8} Torr by a turbo-molecular pump (Varian V-450, 450 L/s). The background pressure was monitored with a Bayard-Albert ionization gauge (Varian 572). The positive ions were detected with a position sensitive detector. The sample mixture was prepared with 10 Torr CF$_2$Br$_2$ (PCR) seeded in 1.5 atm of helium.

Linearly polarized UV laser light (typically 30−100 μJ/pulse) was generated by doubling the Nd:YAG pumped dye laser output (Lumonics HD500) using a BBO crystal and was aligned by using a half-wave retardation plate (CVI co. QWPO-244, 266). The UV laser light was focused perpendicularly onto the molecular beam in the ionization region through a 150-mm focal length lens. The CF$_2$Br$_2$ parent molecules were photolyzed by the UV laser light, and bromine atom fragments were then selectively ionized at 233.9 and 264.8 nm for Br* and at 233.6 and 264.9 nm for Br detection within the same laser pulse using the [2+1] REMPI technique.

Bromine fragment ions were accelerated by a repelling plate with positive high voltage and then passed through extract and ground plates with a 20-mm diameter hole, which caused the nonhomogeneous electric field around the electrode.[20] The
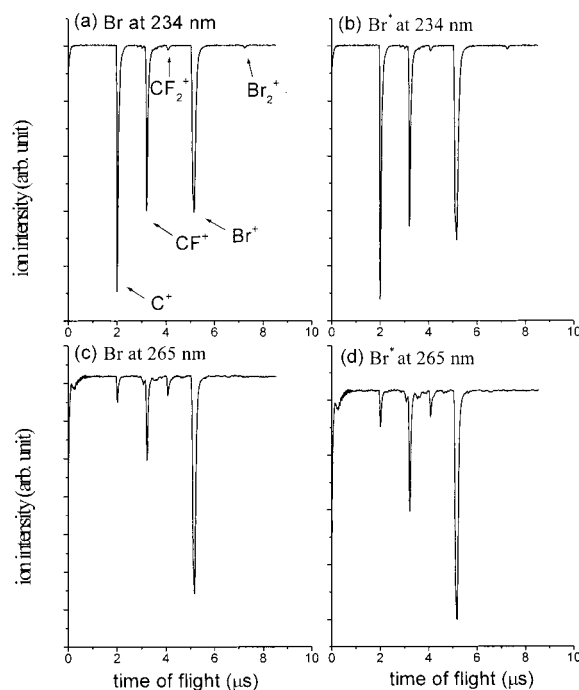

Figure 2. Time-of-flight mass spectra of photofragments in the time range obtained in the 234 (a, b) and 265 nm (c, d) photolysis of CF$_2$Br$_2$. Br$^+$ ion signal formed by the [2+1] REMPI process, while the other peaks result from nonresonant ionization.

bromine ion cloud was expanded spherically due to not only the recoil velocity of the fragments but also the nonhomogeneous electric field. The expansion rate was calibrated against known values obtained in the Br$_2$ and I$_2$ photolysis. The expanded bromine ion cloud was then projected onto a two-dimensional position-sensitive detector composed of a dual-chevron microchannel plate (MCP), a phosphor screen (Galileo Electrooptic Corp. 3040FM), and a charge coupled device (CCD). The MCP signal was sent to the phosphor screen detector to convert the ion signal to the photon signal. A negative high voltage pulse with 150-ns duration was applied to MCP to separate the signal of bromine ion from those of scattered laser light and background ions with different masses. The image was summed over ca. 10 000 shots and the background was removed by subtraction of a reference image collected at an off-resonance wavelength under the same conditions. The REMPI TOF mass spectra were acquired with a photomultiplier tube (Hamamatsu, 1P21) instead of the CCD camera.

3. Results

3.1. TOF Spectra.

The TOF spectra of photofragments in 234-nm photolysis of CF$_2$Br$_2$ were obtained in the range m/e = 0−230 as shown in Figure 2. Five peaks were found in the TOF spectra corresponding to m/e = 12, 31, 50, 80, and 160. The peak at m/e = 80 represents the mixed signal of ^{79}Br$^+$ and ^{81}Br$^+$ formed via REMPI, while the other peaks result from nonresonant processes. The peaks at m/e = 12, 31, and 50 belong to C$^+$, CF$^+$, and CF$_2$$^+$, respectively. The peak at m/e = 160 may be attributed to the mixed signal of ^{79}Br^{79}Br$^+$, ^{79}Br^{81}Br$^+$, and ^{81}Br^{81}Br$^+$, since the natural isotope abundance ratio of ^{79}Br/^{81}Br is 1:1.

TOF spectra in the 265-nm photolysis of CF$_2$Br$_2$ were also obtained. The major difference in the spectra of the 234-nm photolysis is the absence of the molecular bromine ion peak at m/e = 160. Four additional peaks were found at m/e = 12, 31, 50, and 80.
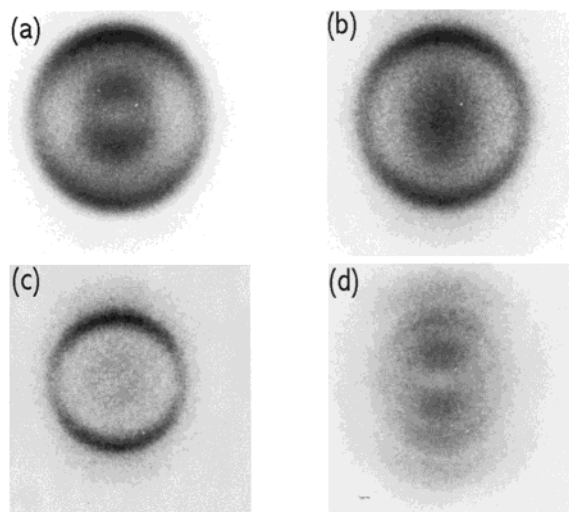
Figure 3. Raw ion images of Br and Br* fragments from the photolysis of CF_2Br_2 at 234 (a, b) and 265 nm (c, d). In all images the linear polarization vector of the photolysis laser is vertical.

3.2. Relative Quantum Yields.

The number density ratio of Br and Br* is proportional to the measured ion signal ratio of the TOF mass spectra and is calculated via eq 1,

$$\frac{N(\text{Br})}{N(\text{Br}^*)} = k\frac{S(\text{Br})}{S(\text{Br}^*)} \tag{1}$$

where $S(\text{Br})$ is the measured ion intensity of Br, $N(\text{Br})$ the number density of Br, and k the proportionality constant. The k value, corresponding to the ionization probability ratio of Br* to Br, was obtained from the Br_2 photolysis under the same experimental condition, since the value of $N(\text{Br})/N(\text{Br}^*)$ is well-known in the Br_2 photodissociation at 234 and 265 nm.[21] The estimated $N(\text{Br})/N(\text{Br}^*)$ values determined via eq 1 were 2.57 $\pm$ 0.29 at 234 nm and 1.12 $\pm$ 0.10 at 265 nm.

Since Br and Br* atoms can be produced through several production channels, the total numbers of species, $N(\text{Br})$ and $N(\text{Br}^*)$, are obtained by summing the numbers of species over the product channels, e.g., the radical, three-body dissociation, and secondary channels.

$$N(\text{Br})_{\text{total}} = N(\text{Br})_{\text{radical}} + N(\text{Br})_{\text{threebody}} + N(\text{Br})_{\text{secondary}} \tag{2}$$

By fitting the speed distribution of Br to the several distribution curves of each channel, the Br ratio of each channel to the total, $N(\text{Br})_{\text{channel}}/N(\text{Br})_{\text{total}}$, was obtained by comparing the areas of the distribution curves. The same method was also applied in the case of the Br* fragment.

3.3. Speed, Translational Energy and Angular Distributions, and Relative Quantum Yields.

The shape and intensity distribution of an image represent the velocity and angular distributions of the photofragments. Figure 3 shows the raw images of two-dimensional projections of the three-dimensional velocity and angular distributions of photofragments. Since the two-dimensional raw image is cylindrically symmetric around the polarization axis of the photolysis laser, a three-dimensional velocity distribution can be reconstructed by performing an inverse Abel transformation.[22] This transformation is very sensitive to noise, therefore the raw images were smoothed with a Gaussian filter with a 5 x 5 pixel window and 2 pixel standard deviation to reduce noise effects in the transformation. Because of the cylindrical symmetry of
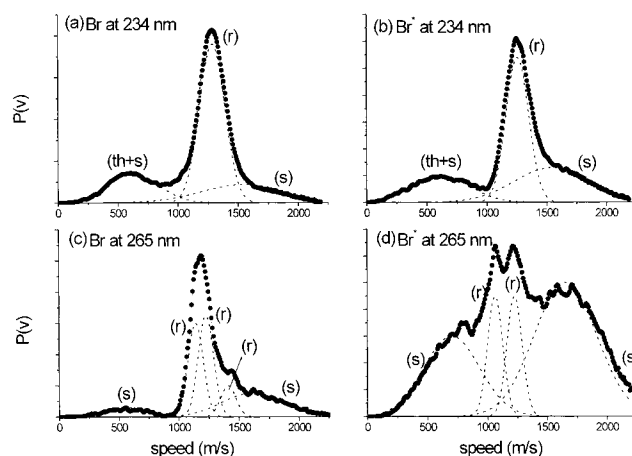

Figure 4. Speed distribution of the Br and Br* fragments for the 234 (a, b) and 265 nm (c, d) photolysis. Small letters in the bracket indicate the origins of the fitted curves; (r), (s), and (th) indicate radical, secondary, and three-body dissociation channels, respectively. The components of the radical channel in (c) and (d) are illustrated in Figure 5.

TABLE 1: Average Translational Energies of Primary Dissociation Channels at 234 nm

channel	E_t, kJ/mol	E_{av}, kJ/mol	FWHM	$\langle f_t \rangle$	Φ^a
$CF_2Br + Br$	106.3	263.8	41.1	0.40	>0.63
$CF_2Br + Br^*$	101.4	219.7	35.6	0.46	>0.21
$CF_2 + Br_2$					trace
$CF_2 + 2Br$		96.4			<0.08
	56.7^b		90.3		
$CF_2 + Br + Br^*$		52.3			<0.05
	51.1		89.9		
$CF_2 + 2Br^*$		8.2			<0.02

^{a} Normalized quantum yields of primary dissociation channels. ^{b} Speed distribution of two channels which overlapped each other.

the velocity distribution, every planar slice containing the symmetry axis is equivalent to the reconstructed images.

The speed distributions, $P(v)$, in Figure 4 were produced by integrating the reconstructed three-dimensional velocity distribution over all angles at each speed. Their resolution is determined to be ca. 7 m/s by the size (equivalent to the number of pixels) of raw images in Figure 3 and is found much better compared to those of TOF in Figure 2. Since Br and Br* atoms are produced through several photodissociation channels, the speed distributions are composed of several distribution curves, which correspond to each channel. The curves were fitted by Gaussian curves. We estimated the origin of the curves by considering the speed, the available energy, the broadness of the curves, and the shapes of the two-dimensional distributions. In general, the speed distribution of the photofragments formed via secondary photodissociation (R4) is broader than one corresponding to the primary photodissociation channels. The available energies of channels are presented in Table 1. The molecular elimination channel was considered to be a very small proportion in the distribution. The Br and Br* speed distributions obtained in the 234-nm photolysis were fitted by three curves, the broad smooth curve comes from the three-body dissociation channel (R3) and the secondary photodissociation channel (R4), the narrow steep curve from the radical channel (R1), and the broad steep curve from the secondary photodissociation channel. In the case of 265-nm photolysis, the three-body dissociation is accessible energetically except the $CF_2 + Br^* + Br^*$ channel. Since the available energy of the $CF_2 + Br + Br^*$ channel is almost zero kilojoules per mole, their peak should be found near zero kilojoules per mole in Figure 4d. However, any experimental peak of the channel was not found in speed distribution. Hence,
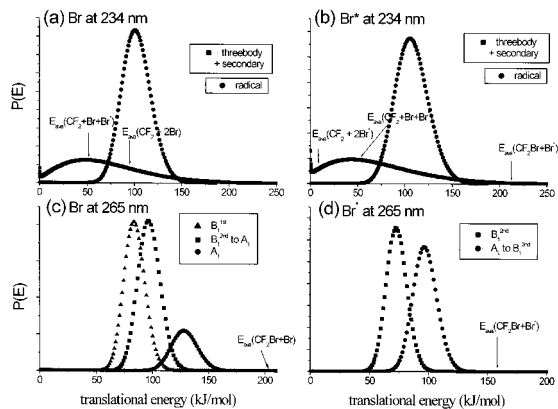
Figure 5. Translational energy distribution of the primary channels at 234 nm (a, b) and components of the radical channel at 265 nm (c, d).

the CF$_2$ + 2Br channel should be the only possible one at 265 nm. The bromine atoms produced through the three-body channel seems to be in the slow part of the speed distribution in Figure 4c because of their small available energy. Although this part may consist of the three-body and the secondary channels, we have spent our main attention to the radical channel at 265 nm because the slow part is negligibly small compared to the total contribution and, hence, the separation of two components is meaningless. The Br speed distribution was fitted by two broad curves representing the secondary channel and three narrow curves representing the radical channel. That of Br* was fitted into two broad and two narrow curves (see Figure 4).

The center of mass translational energies for the radical and three-body dissociation channels were calculated by using eqs 3 and 4, respectively.

$$E_\text{T}(\text{radical}) = \frac{1}{2}(m_\text{Br} + m_{\text{CF}_2\text{Br}})\frac{m_\text{Br}}{m_{\text{CF}_2\text{Br}}}v_\text{Br}^2 \qquad (3)$$

$$E_\text{T}(\text{threebody}) = (m_\text{Br} + 2m_{\text{CF}_2\text{Br}}\cos^2\alpha)\frac{m_\text{Br}}{m_{\text{CF}_2\text{Br}}}v_\text{Br}^2 \quad (4)$$

The translational energy distributions, $P(E)$, in Figure 5 were obtained from the speed distribution by eq 5.

$$P(E) = P(v)\frac{\text{d}v}{\text{d}E} \qquad (5)$$

The available and average internal energies of the CF$_2$Br radical for the radical channel and the CF$_2$ radical for the three-body channel were calculated by using the energy conservation relationship,

$$E_\text{ava} = h\nu - D_0 + E_\text{int}^P \qquad (6)$$

$$E_\text{int} = E_\text{ava} - E_\text{t} - E_\text{el} \qquad (7)$$

where $h\nu$ is the photon energy (452 kJ/mol for the 265 nm and 512 kJ/mol for the 234 nm photolysis wavelengths), D_0 is the dissociation energy of each channel at 0 K, E_int^P is the internal energy of CF$_2$Br$_2$, and E_el is the electronic energy level of the Br atom. E_int^P is assumed to be zero for the supersonic molecular beam. E_el is 0 kJ/mol for Br and 44.1 kJ/mol for Br*. The average translational energies and the relative quantum yields for each primary channel observed in this work are listed in Tables 1 and 2. The contribution of the secondary channel in the quantum yield calculation was not performed since the part is too broadly overlapped to be resolved from the background

TABLE 2: Average Translational Energies of Components of the Radical Channels at 265 nm

channel	origin	E_t, kJ/mol	E_av, kJ/mol	FWHM	$\langle f_t \rangle$	Φ^a
CF$_2$Br + Br	B$_1{}^\text{1st} \rightarrow$ B$_1{}^\text{1st}$	83.8	202.3	22.1	0.41	0.33
	B$_1{}^\text{2nd} \rightarrow$ A$_1$	96.8	202.3	23.8	0.48	0.34
	A$_1 \rightarrow$ A$_1$	128.3	202.3	27.3	0.63	0.11
CF$_2$Br + Br*	B$_1{}^\text{2nd} \rightarrow$ B$_1{}^\text{2nd}$	72.9	158.2	20.6	0.46	0.11
	A$_1 \rightarrow$ B$_1{}^\text{2nd}$	96.8	158.2	23.3	0.61	0.11

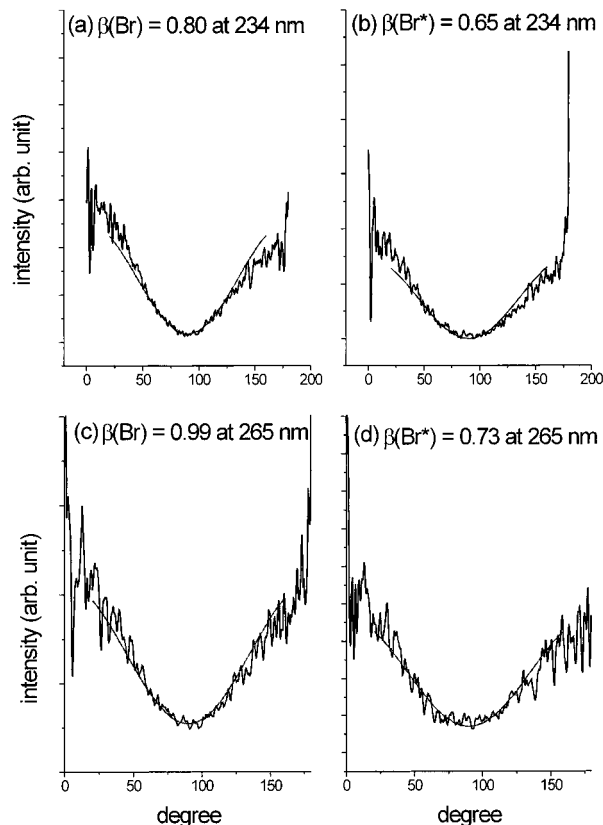^{a} Quantum yields were obtained only for the radical channels.

Figure 6. Angular distributions of the Br and Br* fragments for the 234 (a, b) and 265 nm (c, d) photolysis wavelengths.

noise. The precise description of the contribution is rather premature at the present stage and requires further study.

Figure 5, transformed from Figure 4, shows that more than one-third of the low energy portion exceeds the available energy of the three-body channel and suggests that a considerable amount of bromine fragments formed through the secondary reaction. Consequently, the quantum yield of the three-body channel calculated should be less than the upper limit ratios, i.e., 0.08 for CF$_2$ + 2Br, 0.05 for CF$_2$ + Br +Br*, and 0.02 for CF$_2$ + 2Br*. The two bromine atom formation by one photon was also considered for the quantum yield calculation of the three-body channel.

The angular distribution $P(\theta)$ was obtained by integrating the reconstructed three-dimensional velocity distribution over a proper range of speed at each angle, where θ is the angle between the laser polarization axis and the recoil velocity of the photofragment. To estimate the anisotropy parameter β, $P(\theta)$ was fitted using the standard formula (see Figure 6),

$$P(\theta) \propto 1 + \beta P_2(\cos\theta) \qquad (8)$$

where $P_2(\cos\theta)$ is the second order Legendre polynomial. We calculated the anisotropy parameter only for the radical channel

5610 *J. Phys. Chem. A, Vol. 105, No. 23, 2001*

Park et al.

TABLE 3: Anisotropy Parameters β of the Radical Channels

wavelength, nm	channel	β
234	$CF_2Br + Br$	0.80 (± 0.03)
	$CF_2Br + Br^*$	0.65 (± 0.03)
265	$CF_2Br + Br$	0.99 (± 0.03)
	$CF_2Br + Br^*$	0.73 (± 0.03)

because the distribution of the three-body channel was so broad and was disturbed strongly by background noise and signals from the secondary channel. β values of Br and Br* at 234 nm were calculated for the ranges 1160−1400 and 1135−1360 m/s in Figure 4, parts a and b, respectively. At 265 nm, β values of Br and Br* were extracted only for the components of radical channel which are expected to originate from B_1 states. In the case of Br and Br* at 265 nm, β values were obtained for the ranges 1100−1275 and 985−1140 m/s in Figure 4c,d. (see Table 3).

4. Discussion

The A-band of alkyl halide consists of several electronic transitions to the different dissociative excited states.[23,24] The overlap and curve crossing between the excited-state PESs are the origin of the complex photodissociation dynamics of alkyl halide after A-band excitation. The A-band of CH_2I_2 consists of three components located at 310, 280, and 250 nm, which correspond to B_1, B_1, and A_1 symmetry excited states, respectively.[14,23] For CF_2I_2, the A-band is shifted to slightly longer wavelengths and the B_1, B_1, and A_1 components approach each other. In the case of CF_2Br_2, the close approach of the three components results in a strengthening to make a nearly single Gaussian shaped A-band as in the cases of CF_3Br and CH_3Br. Comparing the molecular symmetry with those of CF_2I_2 and CH_2I_2, B_1(denoted B_1^{1st}), B_1(denoted B_1^{2nd}), and A_1 components of CF_2Br_2 are expected to be in A-band in descending order of wavelengths. The locations of components, however, are not describable due to the broadness and overlap (Figure 1).

Since the anisotropy parameter, β, represents the $\mu \cdot v$ correlation, it is possible to obtain information about the excited states participating in the photodissociation from the β value of the photofragments. The assumed geometry of CF_2Br_2 during the photoexcitation process is C_{2v} with the Br−C−Br moiety on the xz plane. The transition from the ground state, $X(^1A_1)$, may allow access to A_1, B_1, or B_2 symmetric states via the μ_z, μ_x, and μ_y components of the dipole moment operator, respectively. The angles of Br−C−Br and I−C−I, denoted as α, calculated for CF_2Br_2 and CF_2I_2 via RHF/MP2/3-21G level using the GAMESS are 112.5° and 114.7°. When we compare α (=114.7°) of CF_2I_2 with α (=112.5 $\pm$ 0.5°) obtained in electron diffraction studies,[25] α of CF_2Br_2 is expected to be close to 109.5°, which is smaller than that of CF_2I_2 due to its smaller atom size. The angles between the transition dipole moments and Br recoil direction are 54.7°, 35.3°, and 90°, yielding β values of 0, 1, and −1 corresponding to $A_1 \leftarrow X$, $B_1 \leftarrow X$ and $B_2 \leftarrow X$ transitions, respectively.

In Table 3, the β values of Br and Br* formed via the radical channel at 234 nm are 0.80 and 0.65, respectively. These values are close to the limit value of the $\beta = 1$ for a $B_1 \leftarrow X$ transition indicating that this transition is the main photodissociation channel at 234 nm. However, the deviations of β values from the limiting values are too large to be ignored. The differences may be rationalized by the following three arguments. First, the rotation of the molecule during the dissociation reduces the β due to its comparatively shorter rotation period compared to

the dissociation time. Nonetheless, β (=0.99 $\pm$ 0.05) of Br at 265 nm, which is quite close to the limit value, suggests that the dissociation time is very short compared to the rotational period and also indicates that the rotational motion will not affect the β values unless very high rotational levels are populated. Second, the overlap with the nearly isotropic Br photofragments of the secondary product channel may further reduce the value of β. The small β (=0.73 $\pm$ 0.05) of Br* at 265 nm could originate from an overlap between the distribution curves (see Figure 4). In the cases of Br and Br* at 234 nm, the overlap is very small compared to the one at 265 nm. In addition, these two arguments cannot elucidate the difference in β for Br and Br*. The assumption of an $A_1 \leftarrow X$ transition might be a possible explanation since β is zero for such a transition. The difference in β for Br from Br* fragments in the 234-nm photolysis can also be explained by an $A_1 \leftarrow X$ transition. The Br_2^+ ion formed through the molecular elimination channel is another strong evidence for the presence of an $A_1 \leftarrow X$ transition. Since the B_1 excited state is expected to have a nodal plane between the two bromine atoms as in the case of CH_2I_2, a $B_1 \leftarrow X$ transition will not lead to a dissociation into $CF_2 + Br_2$ molecule.[12] If the Br_2 originates from a Br_2 impurity in the sample, it should be in vibrational ground state due to the supersonic expansion conditions. The photodissociation of cold Br_2 molecules at 234 nm is known to produce mainly fast Br atoms ($v_{Br} = 1864$ m/s) and very small amounts of Br_2^+ ions via a nonresonant ionization process.[21] The absence of Br component at $v_{Br} = 1864$ m/s indicates that the origin of the Br_2^+ ion is not due to Br_2 impurities in the sample. Br_2 molecules produced through the molecular elimination channel are expected to be vibrationally hot, because the Br−Br bond contracts during the molecular elimination process. Since there are many bound Rydberg and ion−pair states of Br_2 above 60 000 cm^{-1},[26,27] we suggest that the vibrationally hot Br_2 molecule produced through the molecular elimination channel undergoes a transition to a Rydberg or ion-pair state by absorbing another photon, out of which it is then ionized by absorption of one more photon.

CF_2Br_2 photolysis in the A-band can be complicated by the curve crossing between A_1 and B_1^{2nd} PESs. The correlation diagram between CF_2Br_2 and $CF_2Br + Br(Br^*)$ in C_{2v} symmetry is obtained from the relationship of the point group and the direct productions of the species.[28] $CF_2Br + Br$ correlates with $2A_1$, $2A_2$, $2B_1$, and $2B_2$ states. By matching the states in ascending order of energy, we have found that the A_1 state correlates to $CF_2Br + Br$ diabatically. For the correlation of B_1^{2nd} to $CF_2Br + Br^*$, another B_1 state has been assumed below the B_1^{1st} state, in comparison with the CF_2I_2 case where three B_1 states have been found in the A-band. Two surfaces cross each other due to different symmetries. If the two surfaces are the same symmetries due to symmetry break, an avoided curve crossing occurs between them (see Figure 8). By employing this curve crossing model and eqs 9−11, the crossing probabilities were calculated as listed in Table 4,

$$\beta = X_{B_1^{2nd}}\beta_{B_1^{2nd}} + X_{A_1}\beta_{A_1} =$$
$$X_{B_1^{2nd}}\beta_{B_1^{2nd}}(\beta_{A_1} = 0, X_{B_1^{2nd}} + X_{A_1} = 1) \quad (9)$$

$$P_1 = \frac{\Phi_{Br}(B_1^{2nd} \rightarrow A_1)}{\Phi_{Br^*}(B_1^{2nd}) + \Phi_{Br}(B_1^{2nd} \rightarrow A_1)} \quad (10)$$

$$P_2 = \frac{\Phi_{Br^*}(A_1 \rightarrow B_1^{2nd})}{\Phi_{Br}(A_1) + \Phi_{Br}*(A_1 \rightarrow B_1^{2nd})} \quad (11)$$

where $X_{B_1^{2nd}}$ is the relative fraction originated from the B_1^{2nd}
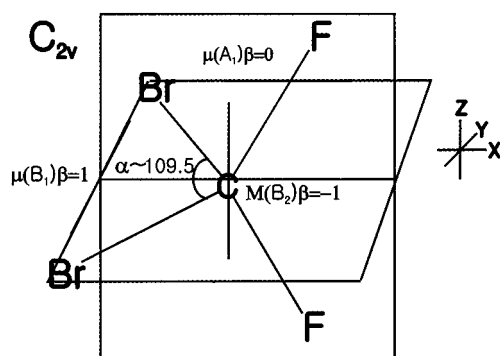
Figure 7. Geometry of the CF$_2$Br$_2$ molecule. The angle α determines the values of the recoil anisotropy parameter β (see text).
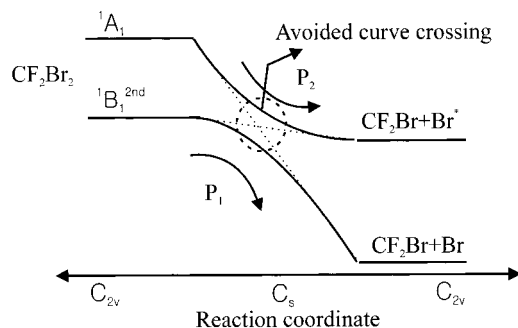

Figure 8. Simple model representing the avoided curve crossing between $^1A_1$ and $^1B_1{}^{2nd}$ potential energy surfaces.

Figure 9. Schematic representation of the three primary photodissociation channels of CF$_2$Br$_2$ at 234 and 265 nm.

PES, $\Phi_{Br}(B_1{}^{2nd} \rightarrow A_1)$ is the relative quantum yield of Br produced by "jumping" from the $B_1{}^{2nd}$ PES to the A_1 PES, and P_1 is the probability of avoided curve crossing in the $B_1{}^{2nd}$ PES. The photodissociation dynamics of CF$_2$Br$_2$ and CF$_3$I in A-band resemble each other. A_1, $B_1{}^{2nd}$, and $B_1{}^{1st}$ correspond to $^1Q_1$, $^3Q_0$, and $^3Q_1$, respectively. In the case of CF$_3$I at 275 nm, the discrepancy of β values, i.e., 1.12 for I and 1.91 for I*, is strong evidence of curve crossing between $^1Q_1$ and $^3Q_0$.[29] In the same manner, the discrepancy of β values of 0.80 for Br and 0.65 for Br* is also strong evidence of curve crossing between A_1 and $B_1{}^{2nd}$ states. On account of the effects of the overlap, the true β of CF$_2$Br + Br at 234 nm is expected to be between 0.8 and 1.0. The P_1 values were calculated for the three cases assuming that the β(Br) values are 0.8, 0.9, and 1.0. With the difference between β(Br) and β(Br*) fixed to 0.15, the P_1 values were estimated to be 0.78. The P_1 value of 0.78 is considerably large compared to those of 0.1–0.4 reported for CF$_3$Br and CH$_3$Br.[30,31] The retainment of C_s symmetry during the dissociation is an important factor to determine the avoided curve crossing probability. By increasing the C–Br bond length during the reaction, the C_{2v} point group changes to C_s, and the symmetries of A_1 and $B_1{}^{2nd}$ PESs become the same, A'. The interaction of two A' PESs results in a strong avoided crossing.
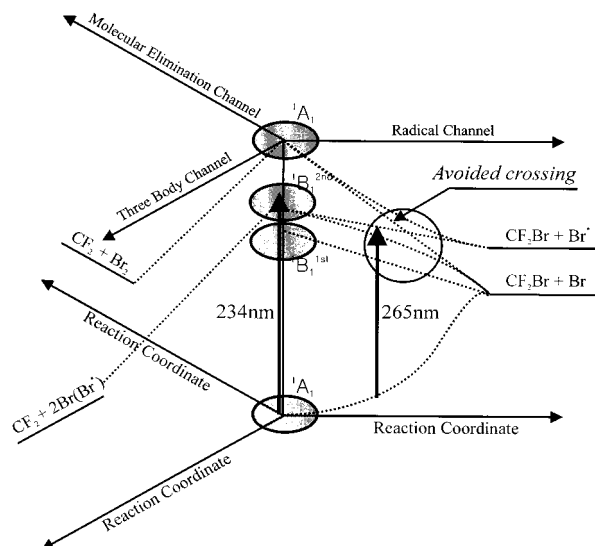
After departure of the Br atom, the CF$_2$Br radical recovers its C_{2v} symmetry. In the cases of CF$_3$Br and CH$_3$Br, although their geometries retain C_s symmetries during dissociation, they are not so departed from C_{3v} symmetries. Hence avoided curve crossing is relatively less probable, whereas in the 234-nm photolysis, the large change in geometry (from C_{2v} to C_s) gives rise to the large avoided curve crossing probability.

In previous photodissociation studies of CH$_2$I$_2$ and CF$_2$I$_2$, the $B_1{}^{1st}$ state has been suggested to be related to the CF$_2$Br + Br channel only.[15,16] The relations between the upper states and the three primary channels, however, are not well understood. We have proposed a simple model (in Figure 9) to explain the correlation between three excited states and three primary dissociation channels. In this model, the CF$_2$Br + Br channel originates from $B_1{}^{1st}$ and A_1 states diabatically and $B_1{}^{2nd}$ state adiabatically by the avoided curve crossing. The CF$_2$Br + Br* channel comes from the $B_1{}^{2nd}$ state diabatically and from the A_1 adiabatically. The molecular elimination channel is scarcely related to the A_1 state at 234 nm (see Table 1). The three-body dissociation channel originates from the $B_1{}^{2nd}$ state and competes with the radical channel. This model is also useful for the photodissociation of CF$_2$I$_2$ in A-band. In the case of CF$_2$I$_2$, the proportion of the $A_1 \leftarrow X$ transition seems not so significant, because of its very small transition probability or because the photolysis wavelength is too long to allow access to the A_1 excited state. The avoided curve crossing between the A_1 and $B_1{}^{2nd}$ PESs and the exclusively high proportion of B_1 excited states can be interpreted in terms of the wavelength dependence of the I/I* branching ratio of the radical channel, the nearly unit β value of the radical channel over all ranges of the A-band,

TABLE 4: Avoided Curve Crossing Probability of A$_1$ and B$_1{}^{2nd}$ Potential Energy Surfaces in the Radical Channel at 234 nm

conditions	$A_1 \rightarrow A_1$	$A_1 \rightarrow B_1{}^{2nd}$	$B_1{}^{2nd} \rightarrow B_1{}^{2nd}$	$B_1{}^{2nd} \rightarrow A_1$	$X(A_1)$	$X(B_1{}^{2nd})$	$P_1{}^a$	P_2
$\beta = 0.80$	0.15			0.61				
					0.23	0.77	0.79	0.35
$\beta* = 0.65$		0.08	0.16					
$\beta = 0.90$	0.08			0.67				
					0.14	0.86	0.78	0.53
$\beta* = 0.75$		0.06	0.19					
$\beta = 1.00$	0			0.75				
					0.04	0.96	0.78	1.00
$\beta* = 0.85$		0.04	0.21					

^{a} P_1 and P_2 are the probabilities of avoided curve crossing in the $B_1{}^{2nd}$ and A_1 PESs.

respectively. Nevertheless, further work is necessary to understand the competition between the three-body dissociation and the radical channel on the B_1^{2nd} state in greater detail.

The transition at 265 nm, the red edge of the A-band, is expected to originate mainly from $B_1^{1st} \leftarrow$ X transition. Figure 4c,d shows that the speed distributions of the CF_2Br + Br and CF_2Br + Br* channels are composed of three and two components, respectively. However, all the components of the speed distributions cannot be assigned completely assuming only two transitions. A complete assignment is possible when we assume the presence of an $A_1 \leftarrow$ X transition at 265 nm. We propose that the origins of the three components are the B_1^{1st}, B_1^{2nd}, and A_1 states and those of two components are the B_1^{2nd} and A_1 states in the ascending order of the translational energy given in Table 2 and Figure 5. Though a 265-nm photon does not provide enough energy to access the A_1 excited-state PES in its equilibrium geometry, an $A_1 \leftarrow$ X transition probably can occur when the electronic state transits close to the curve crossing point. The A_1 excited state approaches the B_1^{2nd} state near the crossing point, and the strong mixing between the two states occurs by symmetry breaking. Therefore a $B_1^{2nd} \leftarrow$ X transition can induce an $A_1 \leftarrow$ X transition when the two excited states are so close that they mix near the curve crossing point. A similar appearance has been found in the case of CF_3I photodissociation at 295 nm, which is too long a wavelength to reach the higher excited state, $^1Q_1$. The transition close to the crossing point near 295 nm produces the mixed recoil anisotropy of the I* fragments because of the strong mixing of the $^3Q_0$ and $^1Q_1$ states.[29] These results suggest that CF_2Br_2 is excited to a position near the curve crossing by absorbing a 265-nm photon. This curve crossing point seems to be located at an energy ca. 38 000 cm^{-1} ($\sim$265 nm) above the ground A_1 state (see Figure 9).

References and Notes

(1) Bromblecombe, P. *Air composition and Chemistry*, 2nd ed.; Cambridge University Press: Cambridge, UK, 1996.

(2) Atkinson, R.; Baulch, D. L.; Cox, R. A.; Hampson, R. F., Jr.; Kerr, J. A.; Troe, J. *J. Phys. Chem. Ref. Data* **1992**, *21*, 1125.

(3) Vatsa, R. K.; Kumar, A.; Naik, P. D.; Rao, K. V. S. R.; Mittal, J. P. *Bull. Chem. Soc. Jpn.* **1995**, *68*, 2817.

(4) Felder, P.; Yang, X.; Baum, G.; Huber, J. R. *Isr. J. Chem.* **1993**, *34*, 33.

(5) Krajnovich, D.; Zhang, Z.; Butler, L.; Lee, Y. T. *J. Phys. Chem.* **1984**, *88*, 4561.

(6) Talukdar, R. K.; Vaghjiani, G. L.; Ravishankara, A. R. *J. Chem. Phys.* **1992**, *96*, 8194.

(7) Wampler, F. B.; Tiee, J. J.; Rice, W. W.; Oldenberg, R. R. *J. Chem. Phys.* **1979**, *71*, 3926.

(8) Sam, C. L.; Yardley, J. T. *Chem. Phys. Lett.* **1979**, *61*, 509.

(9) Abel, B.; Hippler, H.; Longe, N.; Schuppe, J.; Troe, J. *J. Chem. Phys.* **1994**, *101*, 9681.

(10) Gosnell, T. R.; Tayor, A. J.; Lyman, J. L. *J. Chem. Phys.* **1991**, *94*, 5949.

(11) Van Hoeymissen, J.; Peeters, W. V. *J. Chem. Phys. Lett.* **1994**, *226*, 159.

(12) Kawasaki, M.; Lee, S. J.; Bersohn, R. *J. Chem. Phys.* **1975**, *63*, 809.

(13) Kroger, P. M.; Demou, P. C.; Riely, S. J. *J. Chem. Phys.* **1976**, *65*, 1823.

(14) Zhang, J.; Imre, D. G. *J. Chem. Phys.* **1988**, *89*, 309.

(15) Koffend, J. B.; Leone, S. R. *Chem. Phys. Lett.* **1981**, *81*, 136.

(16) Baum, G.; Felder, P.; Huber, J. R. *J. Chem. Phys.* **1993**, *98*, 1999.

(17) Bergmann, K.; Carter, R. T.; Hall, G. E.; Huber, J. R. *J. Chem. Phys.* **1998**, *109*, 474.

(18) Radloff, W.; Farmanara, P.; Stert, V.; Schreiber, E.; Huber, J. R. *Chem. Phys. Lett.* **1998**, *291*, 173.

(19) Kang, W. K.; Kim, Y. S.; Jung, K.-H. *Chem. Phys. Lett.* **1995**, *244*, 183.

(20) Eppink, A. T. J. B.; Parker, D. H. *Rev. Sci. Instrum.* **1997**, *68*, 3477.

(21) Jee, Y. J., private communication.

(22) Candal, S. M. *IEEE Trans. Acoust. Speech, Signal Process.* **1981**, *29*, 963.

(23) Gedanken, A.; Rowe, M. D. *Chem. Phys.* **1979**, *36*, 181.

(24) Gedanken, A. *Chem. Phys. Lett.* **1987**, *137*, 462.

(25) Mack, H. G.; Oberhammer, H.; John, E. O.; Kirchmeier, R. L. *Faraday Discuss. Chem. Soc.* **1967**, *44*, 108.

(26) Ishiwata, T.; Ohtoshi, H.; Tanaka, I. *J. Chem. Phys.* **1984**, *81*, 2300.

(27) Riedly, T.; Lawley, K. P.; Donovan, R. J. *Chem. Phys.* **1990**, *148*, 315.

(28) Herzberg, G. *Molecular spectra and molecular structure,* 1st ed.; National Research Council of Canada, 1966; Vol. III.

(29) Furlan, A.; Gejo, T.; Huber, J. R. *J. Phys. Chem.* **1996**, *100*, 7956.

(30) Thelen, M. A.; Felder, P. *Chem. Phys.* **1996**, *204*, 135.

(31) Gougousi, T.; Samartzis, P. C.; Kitsopoulous, T. N. *J. Chem. Phys.* **1998**, *108*, 5742.